

# BodySLAM: A Generalized Monocular Visual SLAM Framework for Surgical Applications

Guido Manni<sup>a,b,\*</sup>, Clemente Lauretti<sup>b</sup>, Francesco Prata<sup>c</sup>, Rocco Papalia<sup>c</sup>, Loredana Zollo<sup>b</sup> and Paolo Soda<sup>a</sup>

<sup>a</sup>Research Unit of Computer Systems and Bioinformatics, Department of Engineering, Università Campus Bio-Medico di Roma, Rome, Italy,

<sup>b</sup>Unit of Advanced Robotics and Human-Centred Technologies, Department of Engineering, Università Campus Bio-Medico di Roma, Rome, Italy,

<sup>c</sup>Department of Urology, Fondazione Policlinico Universitario Campus Bio-Medico, Rome, Italy,

## ARTICLE INFO

### Keywords:

Endoscopic SLAM  
Monocular depth estimation  
Monocular Pose estimation  
Deep learning  
Surgical navigation

## ABSTRACT

Endoscopic surgery relies on two-dimensional views, posing challenges for surgeons in depth perception and instrument manipulation. While Simultaneous Localization and Mapping (SLAM) has emerged as a promising solution to address these limitations, its implementation in endoscopic procedures presents significant challenges due to hardware limitations, such as the use of a monocular camera and the absence of odometry sensors. This study presents a robust deep learning-based SLAM approach that combines state-of-the-art and newly developed models. It consists of three main parts: the Monocular Pose Estimation Module that introduces a novel unsupervised method based on the CycleGAN architecture, the Monocular Depth Estimation Module that leverages the novel Zoe architecture, and the 3D Reconstruction Module which uses information from the previous models to create a coherent surgical map. The procedure's performance was rigorously evaluated using three publicly available datasets (Hamlyn, EndoSLAM, and SCARED) and benchmarked against two state-of-the-art methods, EndoSFMLearner and EndoDepth. The integration of Zoe in the MDEM demonstrated superior performance compared to state-of-the-art depth estimation algorithms in endoscopy, whereas the novel approach in the MPEM exhibited competitive performance and the lowest inference time. The results showcase the robustness of our approach in laparoscopy, gastroscopy, and colonoscopy, three different scenarios in endoscopic surgery. The proposed SLAM approach has the potential to improve the accuracy and efficiency of endoscopic procedures by providing surgeons with enhanced depth perception and 3D reconstruction capabilities.

## 1. Introduction

Laparoscopy has become the preferred surgical method for various procedures across medical specialties [1]. However, a significant limitation of this technique is its reliance on two-dimensional views [2], and inferring depth from 2D images can be challenging for surgeons and requires years of experience [3].

To address this challenge, there has been growing interest in integrating 3D imaging technology into surgical procedures. Studies have shown that 3D imaging reduces strain on surgeons, enhances procedural performance, and increases the accuracy of instrument manipulation [4, 5]. These benefits lead to better procedural outcomes and shortened learning curves for surgical trainees [6, 7, 8].

In recent years, camera-based tracking and mapping methods have gained popularity in surgical 3D imaging research [1]. Approaches such as mosaicking, Structure from Motion, and Shape from Template have been explored, but they face limitations in the surgical context. Mosaicking stitches together overlapping images to create a comprehensive view of the scene [9, 10, 11]: however, it struggles with illumination variations, camera motion, moving objects, and noise, which can lead to artifacts and reduced visual quality in surgical environments. Structure from Motion reconstructs 3D structures from 2D images taken from different viewpoints [12, 13]: it faces challenges such as

computational complexity, sensitivity to noise and outliers, limited camera calibration, and difficulties handling complex surgical scenes with moving objects, occlusions, and reflections. Shape from Template estimates the 3D shape of a deformable object by aligning a known template to observed images [14, 15], but, it is affected by template size and complexity, image quality and noise, rotation and scaling issues, partial occlusion, and the presence of similar shapes or clutter in surgical scenes.

In contrast, Simultaneous Localization and Mapping (SLAM) has emerged as a promising solution to address these limitations [16, 17, 18]. SLAM algorithms simultaneously estimate the camera pose and construct a map of the environment in real-time, so that they can effectively handle the dynamic and complex nature of surgical scenes, including moving objects, occlusions, and deformations. However, implementing SLAM in endoscopic procedures presents significant challenges. Hardware limitations, such as the use of a monocular camera due to size constraints and the absence of odometry sensors, led SLAM relying solely on visual information for its core processes, such as localization and mapping. Various environmental factors further complicate the application of SLAM, including low-texture surfaces [19], lighting variability [20, 21], organ deformation [22], and the presence of blood, fluids, and smoke [23, 24].

To overcome these limitations in this paper we propose a robust deep learning SLAM approach that effectively works

\*Corresponding author: guido.manni@unicampus.it (G. Manni)

in diverse surgical settings. Our framework combines state-of-the-art and newly developed models, consisting of three main modules:

1. The Monocular Depth Estimation Module (MDEM), which employs a novel deep learning technique that demonstrates exceptional generalization abilities across various imaging contexts.
2. The Monocular Pose Estimation Module (MPEM), using a novel unsupervised method we developed that learns to estimate the relative camera pose between consecutive frames.
3. The 3D Reconstruction Module (3DM), that introduces a multi-phase process that generates point clouds, refines pose estimates, and converts the aligned point clouds into a volumetric representation. The module addresses incremental drift error and scale ambiguity inherent in monocular pose estimation.

To rigorously test our approach and demonstrate its generalization capabilities, we conducted comprehensive evaluations in three surgical environments: laparoscopy, gastroscopy, and colonoscopy. To this end, we used the Hamlyn [17], EndoSlam [16], and SCARED [25] datasets, each offering unique features for validating our proposed method. We also benchmarked our approach against two state-of-the-art methods [17, 16], which are presented in section 5.

The remainder of this paper is organized as follows: section 2 provides an overview of the related work. Section 3 describes our proposed approach, detailing the three primary modules of our framework. Section 4 presents the materials used in this study, including the training, validation, and testing datasets. Section 5 outlines the experimental configuration, including the comparative analysis against the two state-of-the-art approaches, performance metrics, and statistical analysis. Section 6 presents the experimental results. Finally, section 7 provides concluding remarks.

## 2. Related Works

### 2.1. Traditional Monocular Visual SLAM Architecture

A classical Monocular Visual SLAM (MVSLAM) system typically consists of several integrated components, as illustrated in Figure 1A.

The framework begins with a feature extraction module, which identifies salient features (like ORB, SURF, and SIFT [26, 27, 28]) within the images. A feature-matching algorithm then establishes correspondences between these features across consecutive frames. The matched features are passed into a motion estimation algorithm and a depth map estimation algorithm to estimate the relative motion between consecutive frames and generate a sparse depth map, respectively. These outputs are utilized by a map-building algorithm to reconstruct the environmental model. Additionally, the MVSLAM framework incorporates an optimization module, which executes procedures such as bundle adjustment [29] and pose graph optimization to refine the map and pose estimates.

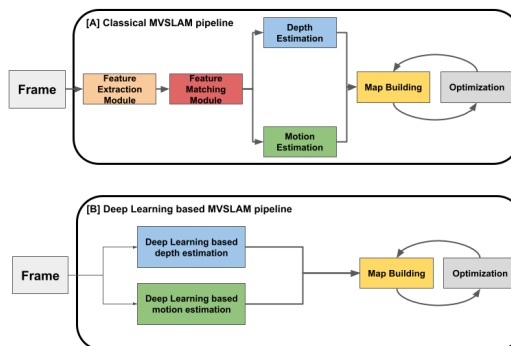


**Figure 1:** Comparison of (A) a classical MVSLAM system and (B) a fully deep learning-based MVSLAM framework. The traditional approach consists of feature extraction, feature matching, motion estimation, depth map estimation, map building, and optimization components. In contrast, the deep learning-based framework replaces conventional algorithms with deep learning models for feature extraction, feature matching, motion estimation, and depth estimation, potentially simplifying the overall architecture complexity.

### 2.2. Challenges and Limitations of Traditional MVSLAM in Endoscopic Surgery

Traditional feature-based methodologies in MVSLAM have encountered notable challenges in the context of endoscopic surgery due to the unique nature of surgical images. Endoscopic images often lack discernible features and are subject to lighting variations, posing substantial difficulties for feature extraction and matching algorithms. For example, a modified version of ORB-SLAM [30], which utilized a limited number of keyframes for dense reconstruction, struggled with soft, texture-less tissue, a common characteristic in Minimally Invasive Surgery (MIS). This highlights the inherent challenge of detecting robust features in environments where texture and contrast are minimal.

Early SLAM techniques, such as those relying on Structure from Motion [31], aimed to concurrently track camera motion and reconstruct the 3D environment. However, these methods were severely limited by the low-texture environments typical of MIS. Structure from Motion relies on robust wide-baseline feature matching, which becomes untenable in texture-deficient surgical scenes. Moreover, the computational expense of Structure from Motion is another drawback, as it requires processing all images collectively to optimize the 3D structures and camera poses, which is not always feasible in real-time surgical applications.

### 2.3. Deep Learning-based MVSLAM Architecture

To address the limitations of traditional MVSLAM methods in endoscopic surgery, researchers have turned to deep learning-based approaches. As shown in Figure 1B, a fully deep learning-based MVSLAM framework replaces the conventional feature matching, feature extraction, motion estimation, and depth estimation algorithms with deep learning models. These models can learn to extract

relevant features and estimate depth and motion directly from the input images, even in the presence of low-texture environments and lighting variations.

Deep learning models offer several advantages over traditional MVSLAM methods in the context of endoscopic surgery. They can adapt to the dynamic, texture-sparse, and unpredictable nature of surgical environments by learning to extract relevant features and estimate depth and motion directly from the data. This eliminates the need for hand-crafted feature detectors and matching algorithms, which often struggle in low-texture environments.

#### 2.4. Advancements in Deep Learning-based MVSLAM for Endoscopic Surgery

Early applications of deep learning in MVSLAM for endoscopic surgery have shown promising results. For example, Chen et al. [32] used Generative Adversarial Networks (GANs) for depth estimation, demonstrating the ability to overcome challenges related to feature scarcity, tissue homogeneity, surface deformation, and highly variable specular appearances.

Hybrid approaches, such as the Endo-Depth-and-Motion framework [17], have attempted to integrate deep learning with traditional techniques. This framework employs MonoDepthV2 [33] for depth estimation and a photometric approach inspired by PTAM [34] for pose estimation. While this approach showed improvements over traditional methods, it still encountered limitations in prolonged tasks, as pose estimation was prone to failure over time.

Fully deep learning-based SLAM systems, such as EndoSLAM [16] for gastroscopy, have further advanced the field by employing deep learning methods for both depth and pose estimation. These approaches have demonstrated the potential of deep learning to provide more robust and adaptable solutions for MVSLAM in the surgical environment.

#### 2.5. Challenges in Deep Learning-based MVSLAM for Endoscopic Surgery

Despite the advancements in deep learning-based MVSLAM for endoscopic surgery, several challenges remain. One major challenge is the need for large amounts of diverse training data to develop models that can generalize well across different surgical scenarios. Collecting and annotating such datasets can be time-consuming and expensive.

Another challenge is the computational complexity of deep learning models, which can hinder real-time performance in resource-constrained surgical environments. Balancing model accuracy and efficiency is crucial for the practical deployment of deep learning-based MVSLAM systems in endoscopic surgery.

#### 2.6. Distinctive Elements of the Proposed MVSLAM Framework

Our proposed MVSLAM framework introduces several distinctive elements that set it apart from the existing literature and address the challenges mentioned above:

1. Integration of the state-of-the-art Zoe model [35] for monocular depth estimation. This model has demonstrated superior generalization capabilities across diverse datasets, enabling our framework to perform well in various surgical scenarios without the need for extensive fine-tuning.
2. A novel pose estimation module, named CyclePose, which leverages the power of Generative Adversarial Networks (GANs) to estimate the relative camera pose between consecutive frames. CyclePose is specifically designed to enhance the accuracy and robustness of pose estimation in the challenging surgical setting, addressing the limitations of previous approaches.
3. A comprehensive 3D reconstruction module that integrates the outputs from the depth and pose estimation modules to generate detailed and coherent 3D models of the surgical scene. The module incorporates several optimization techniques, such as pose graph optimization and the Iterative Closest Point (ICP) algorithm, to refine the pose estimates and enhance the alignment of the reconstructed point clouds. This ensures the generation of accurate and visually appealing 3D models, which can be valuable for surgical planning, guidance, and post-operative analysis.

By introducing these distinctive elements, our proposed MVSLAM framework aims to address the limitations of current methods in endoscopic surgery, such as the inability to handle feature-poor imagery, occlusions by surgical instruments, uniform textures, and variable lighting conditions.

### 3. Methods

The proposed MVSLAM approach is composed of three key modules: the Monocular Depth Estimation Module (MDEM), the Monocular Pose Estimation Module (MPEM), and the 3D Reconstruction Module (3DM), as shown in Figure 2. The structure of the framework is designed to ensure that while the MDEM and MPEM operate independently, their outputs synergistically contribute to the effective functioning of the 3DM. The workflow begins with the MPEM (section 3.1), where the RGB input is processed using CyclePose to estimate the relative motion of the camera between consecutive frames, outputting a motion matrix  $M = [R, t_{unscaled}, 1, 0]$ , where  $R$  is the rotation matrix and  $t_{unscaled}$  is the unscaled translation vector due to the scale ambiguity inherent in monocular pose estimation. Simultaneously, the MDEM (section 3.2) estimates the depth map of the scene from the RGB input. Given that the translation component ( $t_{unscaled}$ ) of the relative motion matrix is unscaled, a dedicated module, comprising a translation estimation module and an Unscented Kalman Filter, is tasked with scale correction. The translation estimation module estimates a scaled translation vector  $t_{scaled}$ , which is then combined with  $t_{unscaled}$  using the UKF to correct the scale of the motion matrix. The 3DM (section 3.3) then employs the outputs from both the MDEM and MPEM. It utilizes the depth map from the MDEM and the pose

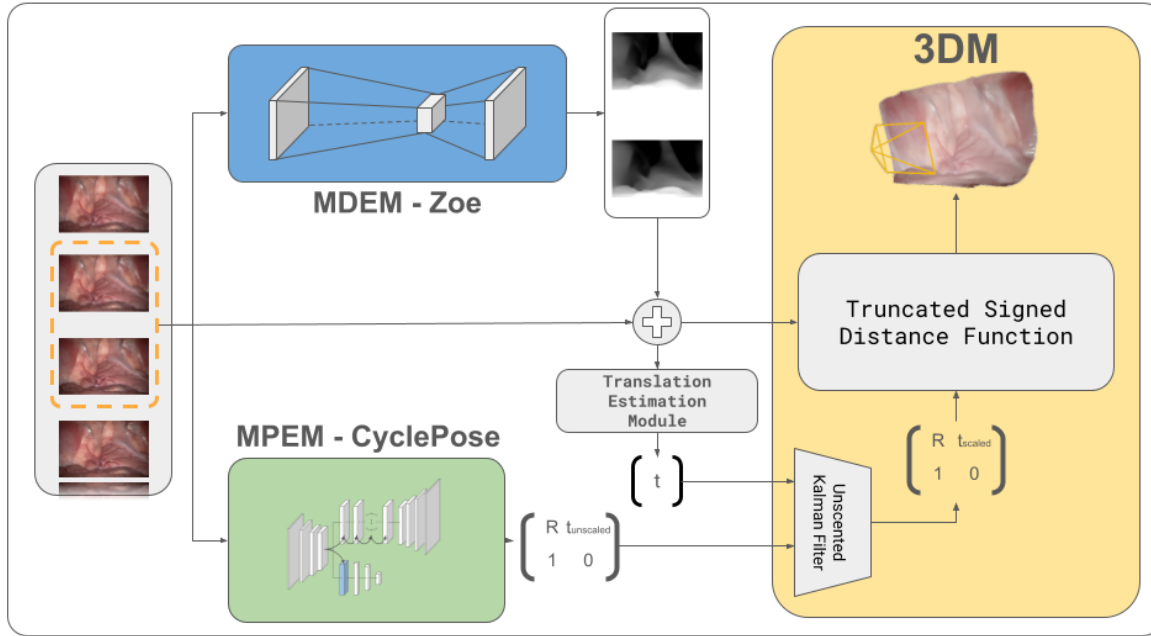


**Figure 2:** The approach takes RGB frames as input and outputs a 3D reconstruction of the surgical scene. The MDEM estimates depth maps from RGB frames, while the MPEM, utilizing CyclePose, computes relative motion between consecutive frames, outputting a motion matrix  $M = [R, t_{\text{unscaled}}, 1, 0]$ , where  $R$  is the rotation matrix and  $t_{\text{unscaled}}$  is the unscaled translation vector. The Translation Estimation Module estimates a scaled translation vector  $t_{\text{scaled}}$ , which is then combined with  $t_{\text{unscaled}}$  using an Unscented Kalman Filter (UKF) to correct the scale of the motion matrix. Finally, the 3DM combines the RGB frames, depth maps, and scaled pose matrices to generate and update the 3D model.

estimations from the MPEM to generate an initial point cloud of the current field of view of the endoscopic camera. This point cloud is carefully merged with the broader scene point cloud, leveraging the pose information to ensure precise alignment and integration.

### 3.1. Monocular Pose Estimation Module (MPEM)

The first step of the approach is based on *CyclePose*, a modified version of CycleGAN, inspired by RetinaGAN [36] and InfoGAN [37]. The main idea is to learn the estimation of the relative camera pose between two consecutive frames, denoted as  $f_{i-1}$  and  $f_i$ , through the pre-task of image-to-image translation in a totally unsupervised manner. We consider this pre-task as a function  $G : f_{i-1} \rightarrow f_i$ , which generates the current frame  $f_i$  from the previous frame  $f_{i-1}$ . Similarly, we define the function  $F : f_i \rightarrow f_{i-1}$ , which generates the previous frame  $f_{i-1}$  from the current frame  $f_i$ . To improve the performance of this image-to-image translation pre-task, we draw inspiration from InfoGAN’s manipulation of the latent space through the maximization of mutual information. We propose to manipulate the latent space  $z$  produced by the generator encoder  $E$  by concatenating a prediction of the relative pose  $M$  between the two consecutive frames to  $z$ . The underlying concept is that if the predicted pose  $M$  is correct, the image-to-image translation task  $G(f_{i-1}, M) \approx f_i$  will also be successful. Conversely, if the estimated pose is incorrect, the pre-task will fail. To accommodate this, the architecture has been modified at the

bottleneck level of the generator architecture (right panel of Figure 3). The modified generator now performs two tasks:

- Predicting the pose  $M$  between two concatenated consecutive frames ( $f_{i-1}$  and  $f_i$ ). This is done by passing the concatenated frame  $f_c = [f_{i-1}, f_i]$  through the generator encoder  $E$ , which then feeds into the pose estimation tail  $P$ . The pose network  $P$  outputs the relative motion matrix  $M$  in quaternion form to avoid gimbal lock and improve numerical stability. The quaternion is immediately converted to a matrix representation  $M = [R, t_{\text{unscaled}}, 1, 0]$ , where  $R$  is the rotation matrix and  $t_{\text{unscaled}}$  is the unscaled translation vector, for better integration within the SLAM pipeline. The final linear layer of the pose network is responsible for outputting  $M$ .
- Generating the next frame (image-to-image translation pre-task). First, the previous frame  $f_{i-1}$  is passed through the encoder  $E$ . The resulting latent space  $z = E(f_{i-1})$  is then concatenated with the predicted pose  $M$  from the first task. This concatenated latent space  $[z, M]$  is then fed into the generator  $G$ , which produces the next frame  $\hat{f}_i = G(z, M)$ .

We now discuss the objective loss function, which has been optimized for the task of pose estimation. The objective function consists of three terms:

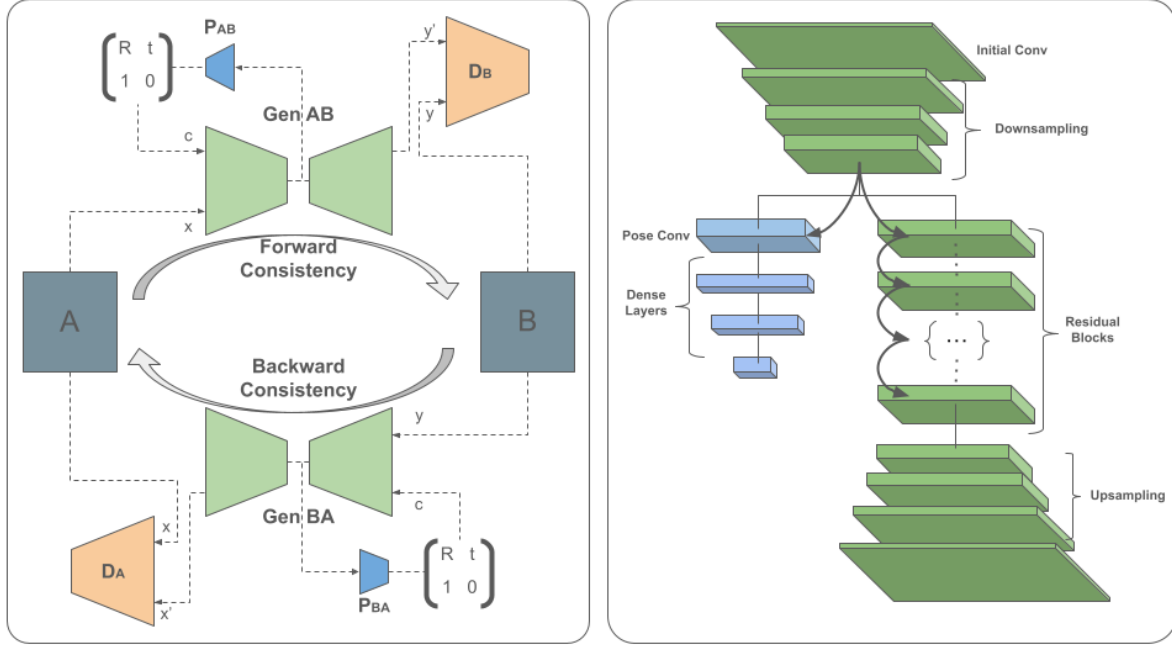


**Figure 3:** Integration of Pose Estimation within the Cycle Consistency Framework and the Neural Network Architecture. *Left:* The diagram illustrates the integration of pose estimation within the Cycle Consistency framework. Generators  $Gen_{AB}$  and  $Gen_{BA}$  perform domain transformations, while pose networks  $P_{AB}$  and  $P_{BA}$  predict the relative pose between consecutive frames. The predicted pose  $M$  is concatenated with the latent space  $z$  to improve image-to-image translation performance. *Right:* The neural network architecture for pose estimation includes convolutional, downsampling, residual, and upsampling layers. The bottleneck is modified to accommodate pose estimation, where the generator encoder  $E$  processes concatenated frames  $f_c = [f_{i-1}, f_i]$  and the pose estimation tail  $P$  produces the relative motion matrix  $M = [R, t_{unscaled}, 1, 0]$ , where  $R$  is the rotation matrix and  $t_{unscaled}$  is the unscaled translation vector. The latent space  $z$  and predicted pose  $M$  are concatenated and fed into the generator  $G$  to produce the next frame  $\hat{f}_i$ .

- The adversarial loss for matching the distribution of generated images to the data distribution in the target domain.
- The cycle consistency loss to prevent the learned mappings on frames  $G$  and  $f$  from contradicting each other.
- The cycle consistency loss on pose to prevent the learned mappings from contradicting each other regarding the estimated pose.

The full objective loss is defined as follows:

$$\begin{aligned} \mathcal{L}(G, F, D_X, D_Y) &= \mathcal{L}_{adv}(G, D_Y, X, Y) \\ &+ \mathcal{L}_{adv}(F, D_X, Y, X) + \lambda_1 \mathcal{L}_{cycImg}(G, F) \\ &+ \lambda_2 \mathcal{L}_{cycPose}(G, F) \end{aligned} \quad (1)$$

where the first two terms,  $\mathcal{L}_{adv}(G, D_Y, X, Y)$  and  $\mathcal{L}_{adv}(F, D_X, Y, X)$ , are the adversarial losses. The third term  $\lambda_1 \mathcal{L}_{cycImg}(G, F)$  is the classical cycle consistency loss on the generated images. The final term  $\lambda_2 \mathcal{L}_{cycPose}(G, F)$  is a custom term added to enforce pose consistency between the estimated poses from the generated images. To enforce pose

consistency, the term  $\mathcal{L}_{cycPose}(G, F)$  is defined as follows:

$$\begin{aligned} \mathcal{L}_{cycPose}(G, F) &= \mathcal{L}_{chordal}(R_{i-1,i}, \hat{R}_{i-1,i}) \\ &+ \mathcal{L}_1(t_{i-1,i}, \hat{t}_{i-1,i}) + \mathcal{L}_{chordal}(R_{i,i-1}, \hat{R}_{i,i-1}) \\ &+ \mathcal{L}_1(t_{i,i-1}, \hat{t}_{i,i-1}) \end{aligned} \quad (2)$$

where  $R_{i-1,i}$  and  $\hat{R}_{i-1,i}$  are the rotation components of the estimated pose between the real frames ( $f_{(i-1)real}, f_{(i)real}$ ) and the generated frames ( $f_{(i-1)recov}, F_{(i)real}$ ), respectively. Similarly,  $t_{i-1,i}$  and  $\hat{t}_{i-1,i}$  are the translation vectors of the estimated pose between the real frames ( $f_{(i-1)real}, f_{(i)real}$ ) and the generated frames ( $f_{(i-1)recov}, f_{(i)real}$ ), respectively. The terms  $R_{i,i-1}$ ,  $\hat{R}_{i,i-1}$ ,  $t_{i,i-1}$ , and  $\hat{t}_{i,i-1}$  are defined analogously for the mapping  $f$ . The chordal loss  $\mathcal{L}_{chordal}$  is defined as:

$$\mathcal{L}_{chordal}(R, \hat{R}) = |R - \hat{R}|_F \quad (3)$$

where  $|\cdot|_F$  denotes the Frobenius norm. The  $\mathcal{L}_1$  loss is defined as:

$$\mathcal{L}_1(t, \hat{t}) = \sum_{i=1}^n |t_i - \hat{t}_i| \quad (4)$$

where  $n$  is the dimension of the translation vector. The chordal loss constrains the rotation component of the estimated relative pose, while the  $\mathcal{L}_1$  loss constrains the translation component.

The overall workflow (left part of Figure 3) is as follows:

- The concatenated frame  $f_c = [F_{i-1}, f_i]$  is passed through the network to predict the relative pose  $M = P(E(F_c))$ .
- The previous frame  $f_{i-1}$  is then passed through the encoder  $E$  for the image-to-image translation task, producing the latent space  $z = E(F_{i-1})$ .
- At the encoder level, the predicted pose  $M$  is concatenated with the latent space  $z$ , resulting in  $[z, M]$ .
- The concatenated latent space  $[z, M]$  is then fed into the generator  $G$ , which produces the next frame  $\hat{F}_i = G(z, M)$ .

### 3.2. Monocular Depth Estimation Module (MDEM)

The Monocular Depth Estimation Module is a crucial component of our MVSLAM approach, responsible for estimating depth from the endoscopic camera frames. Accurate depth estimation is essential for the subsequent 3D reconstruction process.

To address the challenges in monocular depth estimation, particularly generalization across diverse datasets, our MDEM employs the innovative architecture of Zoe [35]. Zoe model utilizes a distinctive two-stage framework:

1. Pre-training on a wide array of datasets for relative depth estimation, which fosters excellent generalization ability.
2. Adding heads for metrics depth estimation and fine-tuning on metrics depth datasets.

This approach allows Zoe to maintain metrics scale while benefiting from the generalization capabilities obtained during the relative depth pre-training phase.

Zoe architecture features a novel metrics bins module, which takes multi-scale features from the MiDaS [38] decoder and predicts bin centres crucial for metrics depth prediction. The module predicts all bin centres at the initial stage and adjusts them at subsequent decoder layers using attractor layers, enabling more accurate and adaptable depth estimation.

Another innovative aspect of Zoe is its use of the log-binomial method for final metrics depth prediction, instead of the conventional softmax approach. This method linearly combines the bin centres, weighted by their probability scores, enhancing the model’s ability to accurately predict depth in a structured and ordered manner.

Integrating Zoe into our MVSLAM approach represents a significant advancement in-depth estimation for endoscopic applications. Its architecture, combining the strengths of relative and metrics depth estimation and utilizing novel components, makes it exceptionally suited for the challenging and variable conditions of endoscopic surgery.

In our approach, we chose to assess Zoe’s out-of-the-box performance to evaluate its generalization capabilities across domains, without retraining or fine-tuning the model specifically for the surgical context (section 6.2).

### 3.3. 3D Reconstruction Module (3DM)

The 3D reconstruction module generates three-dimensional models from endoscopic images through a multi-phase process. The key steps involved are:

1. Constructing a point cloud from the endoscopic camera perspective using pseudo-RGBD frames produced by the MDEM.
2. Refining the pose estimate provided by the MPEM through multiple optimization steps.
3. Aligning and integrating the newly acquired point cloud with the pre-existing reconstructed scene, guided by the refined pose estimate.

One of the critical aspects of this module is the optimization procedures applied to enhance the pose estimate derived from the MPEM. The raw pose estimate cannot be directly employed for point cloud alignment and merging due to scale ambiguity inherent in monocular pose estimation.

To address this issue, a dedicated sub-module for scale correction has been implemented. This sub-module employs a classical pose estimation algorithm that leverages features extracted (SIFT or ORB) from pseudo-RGBD frames to estimate a pose. Although less effective for pose estimation in low-texture environments, it is viable for deriving a pseudo-scale.

An Unscented Kalman Filter (UKF) is utilized to fuse the unscaled translation vector  $t_{unscaled}$  obtained from the MPEM with the scaled translation vector  $t_{scaled}$  estimated by the translation estimation module. The state vector of the UKF is defined as:

$$x = [t_x, t_y, t_z]^T \quad (5)$$

where  $t_x$ ,  $t_y$ , and  $t_z$  are the components of the translation vector. The measurement model of the UKF is given by:

$$z = [t_{scaled_x}, t_{scaled_y}, t_{scaled_z}]^T \quad (6)$$

where  $t_{scaled_x}$ ,  $t_{scaled_y}$ , and  $t_{scaled_z}$  are the components of the scaled translation vector obtained from the RGB-D odometry or the scaling factor computation.

The UKF operates in two main steps:

1. prediction step: The UKF predicts the next state  $\hat{x}$  using the unscaled translation vector  $t_{unscaled}$  obtained from the MPEM:

$$\hat{x} = f(x, t_{unscaled}) \quad (7)$$

where  $f$  is the state transition function that uses the MPEM to predict the next state.

2. Update step: The UKF updates the predicted state  $\hat{x}$  using the scaled translation vector  $t_{scaled}$  obtained from the RGB-D odometry or the scaling factor computation:

$$x = \hat{x} + K(z - h(\hat{x})) \quad (8)$$

where  $K$  is the Kalman gain,  $z$  is the measurement vector containing the scaled translation, and  $h$  is the measurement function that maps the predicted state to the measurement space.

Dataset	Depth	Pose	Procedure	Frames
Hamlyn [17]	✓		Laparoscopy	78,160
EndoSLAM [16]		✓	Gastroscopy, Colonoscopy	76,837
SCARED [25]	✓	✓	Laparoscopy	17,206

**Table 1**

Overview of endoscopic datasets used for evaluating depth estimation and pose estimation modules in MVSLAM framework. Checkmarks indicate the specific modules tested on each dataset

The corrected translation vector  $t_{corrected}$  is then obtained from the updated state of the UKF:

$$t_{corrected} = [x_1, x_2, x_3]^T \quad (9)$$

where  $x_1$ ,  $x_2$ , and  $x_3$  are the scaled translation components of the updated state vector.

The corrected translation vector  $t_{corrected}$  is used to update the motion matrix  $M$  obtained from the MPEM, resulting in a scaled motion matrix  $M_{scaled}$ :

$$M_{scaled} = [R, t_{corrected}, 1, 0] \quad (10)$$

where  $R$  is the rotation matrix obtained from the MPEM. Additionally, pose graph optimization is periodically employed to mitigate the cumulative effect of drift by evenly distributing the error across all estimated poses. Upon aligning the point cloud, the module utilizes the Truncated Signed Distance Function (TSDF) [39] technique to convert the point cloud data into a comprehensive volumetric representation. The TSDF is a volumetric representation that stores the signed distance to the nearest surface at each voxel. It allows for efficient fusion of depth information from multiple viewpoints and enables the generation of a smooth and continuous surface reconstruction. The scene is partitioned into voxels, each storing a cumulative signed distance function. This voxel-based approach is continually updated through sequential averaging, reflecting the most current information captured by the endoscopic camera.

## 4. Materials

In this study, we employed a comprehensive approach to train, validate, and test our proposed method, utilizing the diverse datasets listed in table 1 to ensure robustness and generalizability in endoscopic applications.

### 4.1. Training Datasets for CyclePose

The training and validation processes were performed on the CyclePose module because it was the only model we trained in this study. Two distinct datasets were utilized - an extensive internal dataset for training and selected subsets from the EndoSLAM dataset [16] for validation. For training, we leveraged a large internal unlabeled dataset comprising more than 300 hours of gastroscopy and prostatectomy videos, collected from 100 patients undergoing these procedures at Fondazione Policlinico Universitario Campus Bio-Medico. In total, this training dataset contained

2,250,900 frames, allowing us to effectively train our pose estimation network on a substantial amount of endoscopic data. To prepare the training data, we processed the videos by extracting individual frames and performing a center crop of size 128x128 pixels on each frame. This center cropping approach enhances system robustness by training it to work effectively with a reduced receptive field, while avoiding any distortion that may arise from resizing the frames. By focusing on the central region of each frame, we ensure that the most relevant visual information is preserved while maintaining the spatial integrity of the data. To validate CyclePose, we used the following subsets from the EndoSLAM dataset, which are completely separate from the training data: HighCam Colon IV Tumor-Free Trajectory 1, LowCam Colon IV Tumor-Free Trajectory 1, HighCam Colon IV Tumor-Free Trajectory 5, and LowCam Colon IV Tumor-Free Trajectory 5. These subsets account for four video sequences with a total of 3024 frames, providing a diverse range of scenarios to assess CyclePose’s inference performance. Importantly, there is no overlap between the training and validation datasets, as the EndoSLAM subsets were specifically chosen for validation purposes only and were not used in any way during the training phase.

### 4.2. Testing Datasets for Depth and Pose Estimation Modules

To evaluate the performance of our depth estimation and pose estimation modules we utilized three datasets with distinct characteristics, as summarized in Table 1. They are:

1. Hamlyn Dataset [17]: We employed an enhanced version of the Hamlyn dataset, which contains stereo images from endoscopic interventions on porcines. This dataset, augmented with depth ground truth derived from stereo images using Libelas, consists of 78,160 frames across 20 videos, making it suitable for testing the depth estimation module of our method. However, it lacks pose ground truth, limiting its utility for assessing the pose estimation module.
2. EndoSLAM Dataset [16]: In addition to its use in validating CyclePose, the EndoSLAM dataset was also employed for testing the pose estimation module of our method. The subsets used for validating CyclePose were excluded from the testing process to maintain a clear separation between validation and testing data. While the EndoSLAM dataset includes depth data, we did not use it for testing depth estimation due to its synthetic nature. The dataset comprises both ex-vivo and synthetic porcine data, with 35 sub-datasets totaling 76,837 frames spanning various gastrointestinal areas, providing pose data for a comprehensive evaluation of our method’s performance in pose estimation.
3. SCARED Dataset [25]: The SCARED dataset, recorded using a da Vinci Xi surgical robot, consists of 7 training and 2 test sets, each corresponding to a single porcine subject. Each set contains 4 to 5 keyframes representing distinct scene views, with structured light

patterns projected for dense stereo reconstruction. The movement of the endoscope enabled the capture of camera poses relative to the robot base, and the projection of 10-bit Gray code patterns onto the scene ensured unique pixel encoding for efficient stereo matching and depth recovery. The SCARED dataset provides both depth maps and ground truth poses, making it suitable for testing both the depth and pose estimation modules of our method.

By leveraging these diverse datasets, we were able to thoroughly test our depth estimation and pose estimation modules across various scenarios and data types, ensuring their robustness and generalizability in endoscopic applications.

## 5. Experimental Configuration

To validate the effectiveness and generalization capabilities of our proposed MVSLAM approach, we conducted a comprehensive comparative analysis against two state-of-the-art approaches [1] in the field of endoscopic surgery: EndoSLAM [16] and EndoDepth [17]. These methods were selected based on their proven performance and distinct approaches to addressing the challenges inherent in endoscopic imagery. EndoSLAM, also known as EndoSfMLearner, is an unsupervised monocular visual odometry and depth estimation approach designed specifically for endoscopic videos. It focuses on depth estimation, pose estimation, and 3D reconstruction. The depth estimation component, based on [40], predicts dense disparity maps from single images using spatial attention mechanisms and a hybrid loss function. The pose estimation component calculates the relative 6-DoF camera poses between consecutive image frames, leveraging a spatial attention block (ESAB) to emphasize texture details and depth differences.

EndoDepth presents a comprehensive approach for 3D reconstruction and camera motion estimation in monocular endoscopic sequences. It utilizes self-supervised depth networks, photometric tracking, and volumetric fusion to generate pseudo-RGBD frames, track the camera pose, and fuse registered depth maps into a coherent 3D scene model. The depth estimation component employs the Monodepth2 [33] network architecture, which is self-supervised and operates on a U-Net encoder-decoder structure with a ResNet18 encoder. Both EndoSLAM and EndoDepth were utilized as developed by their respective authors, without any modifications or retraining. The training and validation contexts of these models are also significant. EndoDepth validation on the Hamlyn Dataset and EndoSLAM on the EndoSLAM dataset provide a varied baseline for assessing the generalization capabilities of our proposed MVSLAM approach.

### 5.1. Performance Metrics and Statistical Analysis

To evaluate the performance of the SLAM approach, we employed a set of well-established metrics for depth estimation and pose estimation. For depth estimation, we selected the Absolute Relative Difference (Abs, Rel. Diff),

Metric	Formula	Description
Abs. Rel. Diff.	$\frac{1}{N} \sum_{i=1}^N \frac{ d_i^p - d_i^t }{d_i^t}$	Average of relative depth prediction errors
Sq. Rel.	$\frac{1}{N} \sum_{i=1}^N \left( \frac{d_i^p - d_i^t}{d_i^t} \right)^2$	Emphasizes larger errors by squaring relative error
RMSE	$\sqrt{\frac{1}{N} \sum_{i=1}^N (d_i^p - d_i^t)^2}$	Standard deviation of errors, weights larger errors more
RMSE-Log	$\sqrt{\frac{1}{N} \sum_{i=1}^N (\log d_i^p - \log d_i^t)^2}$	Evaluates errors in log scale, for wide depth ranges
Accuracy( $\delta$ )	$\frac{1}{N} \sum_{i=1}^N \left[ \max \left( \frac{d_i^p}{d_i^t}, \frac{d_i^t}{d_i^p} \right) < \delta \right]$	Proportion of predictions within factor $\delta$ of true values

**Table 2**

Key Metrics for Evaluating Depth Prediction Accuracy.  $d^p$ : predicted depth,  $d^t$ : true depth.

Metric	Formula	Description
ATE	$\ \text{trans}(E_{ij})\ $	Magnitude of translational pose error, capturing overall trajectory deviation
RTE	$\ \text{trans}(E_{ij})\ $	Translational error over trajectory segments, assessing local consistency and drift
RRE	$ \text{angle}(\log_{S^3}(\text{rot}(E_{ij}))) $	Angular deviation in rotation component, indicating rotational drift

**Table 3**

Trajectory Evaluation Metrics (evo Implementation).  $E_{ij}$ : pose error between estimated and ground truth poses.  $\text{trans}(E_{ij})$ : translational component,  $\text{angle}(\cdot)$ : angular difference from rotational data. ATE: Absolute Trajectory Error, RTE: Relative Trajectory Error, RRE: Relative Rotation Error.

Root Mean Square Error (RMSE), RMSE log, Squared Relative Error (Sq. Rel.), and accuracy thresholds of 1.25, 1.25<sup>2</sup>, and 1.25<sup>3</sup>, as described in [41] and presented in Table 2. To measure the pose estimation performance, we utilized the Relative Translation Error (RTE), Relative Rotation Error (RRE), and Absolute Translation Error (ATE), as shown in Table 3. These metrics are widely used in the literature for evaluating the accuracy of pose estimation in SLAM systems [1]. In addition to the performance metrics, we conducted a statistical analysis to determine the significance of the performance differences observed between the MVSLAM approach and the benchmark models across various scenarios. We verified that the data for each model meets the assumptions required for using an independent two-sample T-test, including normality and equal variances. We then performed pairwise comparisons between the MVSLAM approach and each benchmark model separately, using a significance level of  $p = 0.05$ .



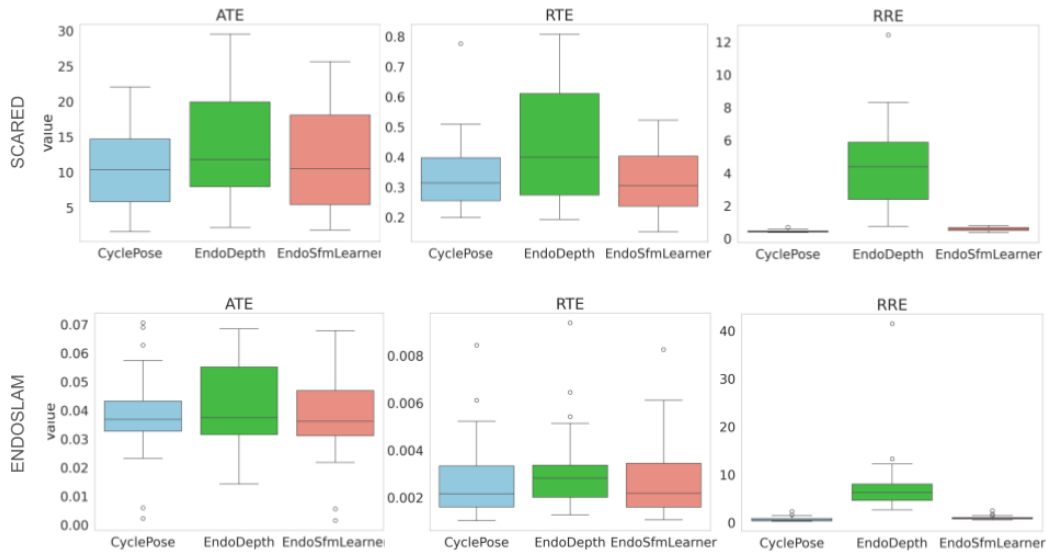


**Figure 4:** Comparison of the performance of CyclePose, EndoDepth, and EndoSfmLearner algorithms on the SCARED and ENDOSLAM datasets. Metrics evaluated include Absolute Trajectory Error (ATE), Relative Trajectory Error (RTE), and Relative Rotation Error (RRE). Each box plot shows the distribution of the errors for the respective algorithms, highlighting the median, interquartile range, and outliers.

## 6. Results

In this section, we present the results of our comprehensive evaluation aimed at validating the efficacy and robustness of our proposed MVSLAM approach. Initially, in section 6.1, we provide an analysis of the monocular pose estimation module. This is followed by section 6.2, where we explore the application and validation of the depth estimation module. It should be noted that the 3D Mapping Module (3DM) cannot be directly evaluated due to two key factors. First, the lack of ground truth 3D models for the tested environments hinders a comprehensive validation of the reconstruction quality. Second, even if ground truth 3D models were available, the scale ambiguity inherent in the monocular pose and depth estimation modules would render the reconstructed model incomparable due to differing scales. However, this inability to directly evaluate the 3DM does not represent a limitation of our approach. The 3DM employs state-of-the-art 3D reconstruction algorithms that have been rigorously tested and validated in prior work [39, 42]. Furthermore, the 3D mapping and localization capabilities critically depend on the performance of the pose estimation and depth estimation modules, which are thoroughly evaluated in the following sections. The successful functioning of the overall SLAM system thus implicitly validates the efficacy of the 3DM.

### 6.1. Monocular Pose Estimation Module (MPem)

Figure 4 presents the performances of the monocular pose estimation module measured in terms of ATE, RTE, and RRE on the two datasets (SCARED and EndoSLAM) when adopting each of the three methods, i.e., CyclePose, EndoSfmLearner and EndoDepth.

In the case of trajectory errors, being either an absolute or a relative error, both rows show that CyclePose and EndoSfmLearner have lower median scores and interquartile ranges than EndoDepth. The figure compares the three methods across the two datasets and three metrics. The rows represent the SCARED and ENDOSLAM datasets, while the columns show the ATE, RTE, and RRE metrics respectively. Regarding the statistical analysis, Table 4 shows there none of these methods has a performance that is statistically different from the other two. It is also interesting to note that our CyclePose approach not only performs as the others but it also has the lowest inference time (Table 5).

Turning our attention to RRE, i.e., a score measuring the angular deviation in the rotation component, we notice that CyclePose outperforms both EndoSfmLearner and EndoDepth on both datasets (both rows and last column of Figure 4). Furthermore, these performance differences are also statistically significant (last rows for both datasets of Figure 4). To deepen the results we also perform an ablation study that aims to investigate the effectiveness of the new terms that we introduced for the cycle loss (section 3.1). To this end, we ran four experiments, two per dataset, setting  $\lambda_2 \neq 0$ ,  $\lambda_2 = 0$  (Figure 5). Both in the case of trajectory errors, being either an absolute or a relative error, and the relative rotation error, both rows show that the model with the new term ( $\lambda_2 \neq 0$ ) has lower median scores and interquartile ranges than the counterpart without the custom term ( $\lambda_2 = 0$ ).

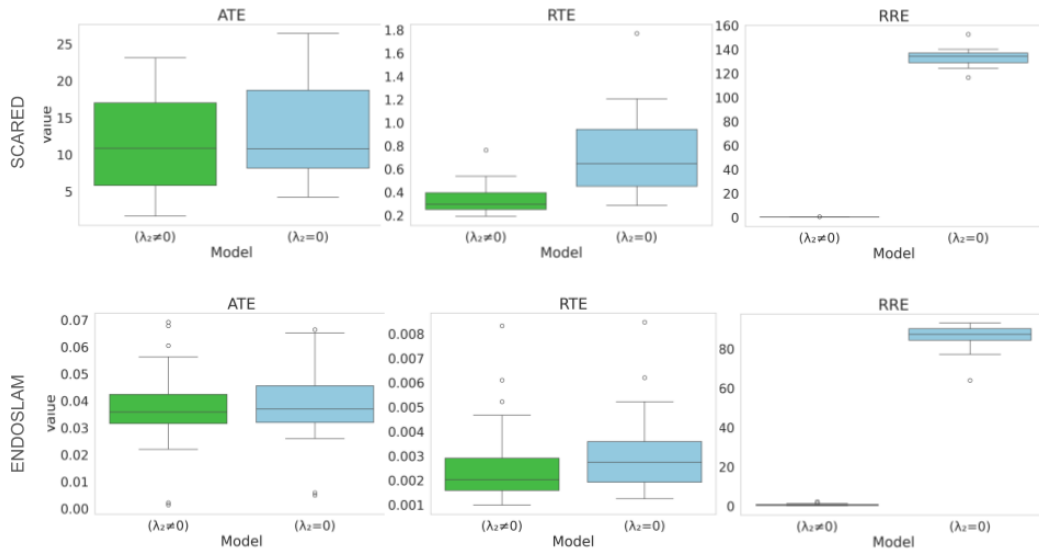


**Figure 5:** Ablation study of cycle loss term modifications. This figure presents the impact of different cycle loss term settings ( $\lambda_2 \neq 0$  vs  $\lambda_2 = 0$ ) on the performance of models evaluated on the SCARED and ENDOSLAM datasets. The metrics assessed include Absolute Trajectory Error (ATE), Relative Trajectory Error (RTE), and Relative Rotation Error (RRE). Each box plot illustrates the distribution of the errors for the respective models, highlighting the median, interquartile range, and outliers.

DS	Metric	Comparison	T-Stat	P-Value
SCARED	ATE	BodySLAM vs EndoDepth	-1.12	0.2693
		BodySLAM vs EndoSFMLearner	-0.59	0.5593
	RTE	BodySLAM vs EndoDepth	-1.65	0.1075
		BodySLAM vs EndoSFMLearner	0.63	0.5334
	RRE	BodySLAM vs EndoDepth	-6.23	<b>6.99e-06</b>
		BodySLAM vs EndoSFMLearner	-3.53	<b>0.0014</b>
ENDOSLAM	ATE	BodySLAM vs EndoDepth	-1.02	0.3121
		BodySLAM vs EndoSFMLearner	-0.12	0.9087
	RTE	BodySLAM vs EndoDepth	-1.29	0.2012
		BodySLAM vs EndoSFMLearner	-0.01	0.9941
	RRE	BodySLAM vs EndoDepth	-7.59	<b>1.73e-09</b>
		BodySLAM vs EndoSFMLearner	-3.85	<b>0.0002</b>

**Table 4**

Comparative analysis of BodySLAM against EndoDepth and EndoSFMLearner across different metrics (ATE, RTE, RRE) for SCARED and ENDOSLAM datasets. T-Statistic and P-Value are reported for each comparison. Bold P-Values indicate statistically significant differences ( $p < 0.05$ ).

## 6.2. Monocular Depth Estimation Module (MDEM)

Figure 6, 7 present the performances of the monocular depth estimation module, BodySLAM, compared to EndoDepth and EndoSfmLearner respectively on the Hamlyn and SCARED datasets. The figures compare the three methods across multiple evaluation metrics for each dataset. The x-axis represents the different methods (BodySLAM, EndoDepth, and EndoSfmLearner), while the y-axis shows

Model	Dataset	Time [s]
EndoSFMLearner	EndoSLAM	38.95
	SCARED	97.72
CyclePose	EndoSLAM	<b>3.32</b>
	SCARED	<b>38.57</b>
EndoDepth	EndoSLAM	1140.56
	SCARED	934.18

**Table 5**

Comparison of models, datasets, and execution times. This table presents the processing times for different models across two datasets, EndoSLAM and SCARED, highlighting the computational efficiency of each approach. All computations were performed on an NVIDIA RTX 3070 GPU.

the values for the evaluation metrics. In the case of the Hamlyn dataset (Figure 6), BodySLAM outperforms both EndoDepth and EndoSfmLearner across all metrics. For Absolute relative difference, RMSE, RMSE log and Squared Relative error (first row, Figure 6), BodySLAM exhibits lower median values and smaller interquartile ranges compared to the other methods. Regarding the threshold accuracy (second row, Figure 6), where values close to or equal to 1 are considered optimal, BodySLAM shows a median closest to this optimal value and a smaller interquartile range compared to the others. Similarly, for the SCARED dataset (Figure 7), BodySLAM outperforms EndoDepth and EndoSfmLearner across all metrics. As with the Hamlyn dataset, BodySLAM demonstrates lower median values and smaller interquartile ranges for Absolute relative difference, RMSE, RMSE log and Squared Relative error (first row,

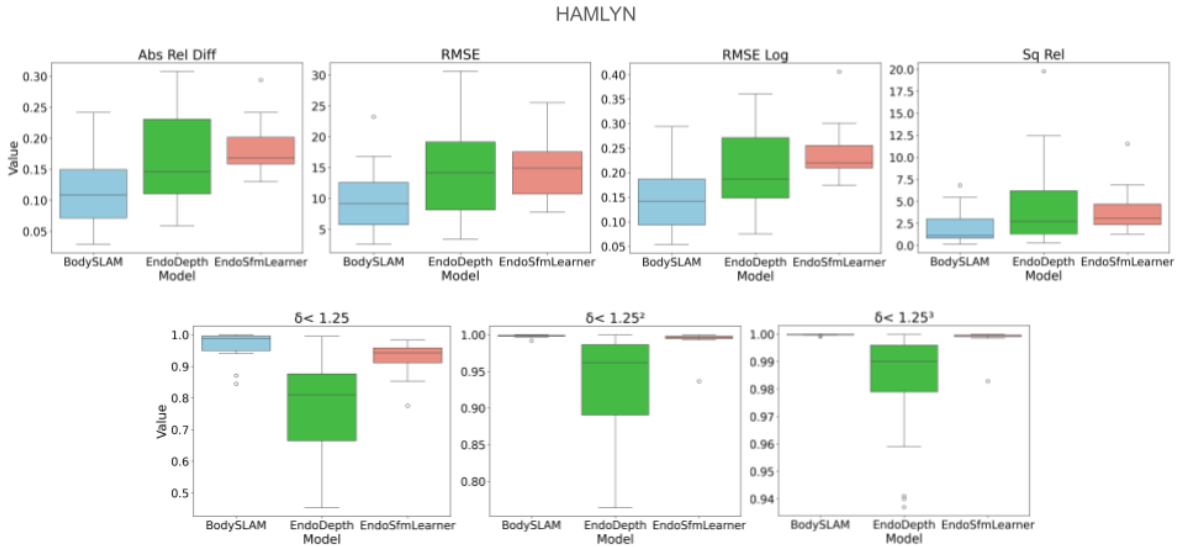


**Figure 6:** Comparison of depth estimation performance for BodySLAM, EndoSfmLearner, and EndoDepth across various metrics on Hamlyn Dataset. Box plots show that BodySLAM achieves the best performance with the lowest median values for absolute relative difference, RMSE, RMSE log, and squared relative difference, and the highest median values for accuracy thresholds  $\delta < 1.25$ ,  $\delta < 1.25^2$ , and  $\delta < 1.25^3$ . EndoSfmLearner demonstrates the second best performance, while EndoDepth shows the poorest results among the three methods compared.

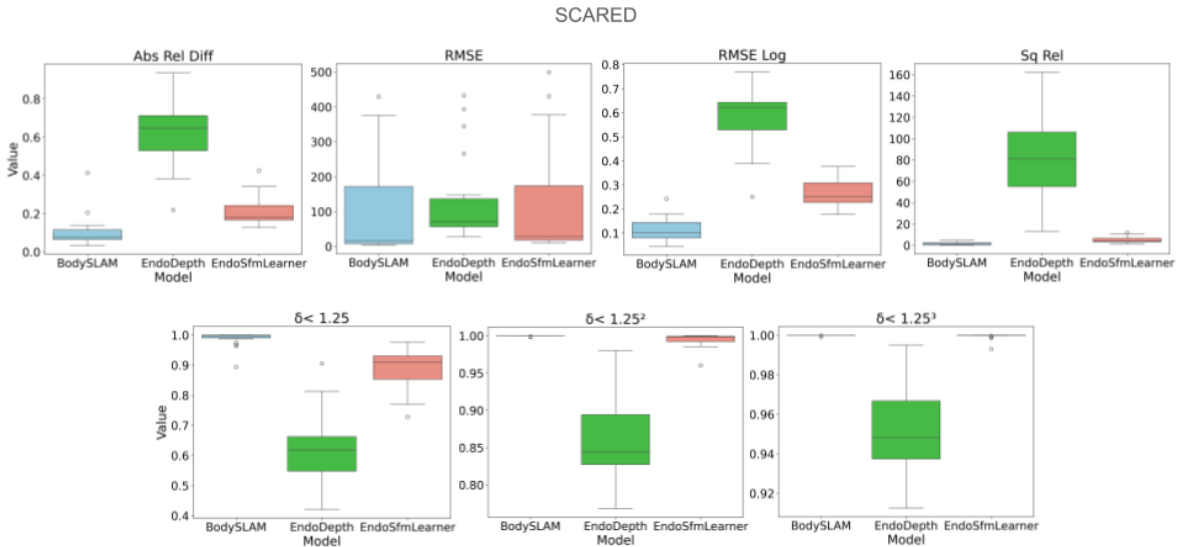


**Figure 7:** Comparison of depth estimation performance for BodySLAM, EndoSfmLearner, and EndoDepth across various metrics on Hamlyn Dataset. Box plots show that BodySLAM achieves the best performance with the lowest median values for absolute relative difference, RMSE, RMSE log, and squared relative difference, and the highest median values for accuracy thresholds  $\delta < 1.25$ ,  $\delta < 1.25^2$ , and  $\delta < 1.25^3$ . EndoSfmLearner demonstrates the second best performance, while EndoDepth shows the poorest results among the three methods compared. Outliers beyond 1.5 times the interquartile range from the quartiles have been excluded to enhance clarity and focus on the central trends of the data.

Figure 7). For the threshold accuracy (second row, Figure 7), BodySLAM median is closest to the optimal value of 1, with a smaller interquartile range compared to the other methods. To deepen the results we also performed a statistical analysis presented in Table 6 for the Hamlyn dataset and in Table 7 for the SCARED Dataset.

The statistical analysis presented on the Hamlyn dataset shows that BodySLAM outperforms the other depth estimation models, except for the threshold accuracy  $(1.25)^2$  and  $(1.25)^3$ , where BodySLAM does not significantly outperform EndoSfmLearner. For the SCARED dataset, BodySLAM outperforms the other depth estimation models in most metrics. However, there are a few exceptions: in

Metric	Comparison	T-Stat	P-Value
Absolute Relative Difference	BodySLAM vs EndoDepth	-2.18	<b>0.0362</b>
	BodySLAM vs EndoSFMLearner	-4.24	<b>0.0001</b>
RMSE	BodySLAM vs EndoDepth	-1.99	0.0536
	BodySLAM vs EndoSFMLearner	-2.86	<b>0.0069</b>
RMSE Log	BodySLAM vs EndoDepth	-2.13	<b>0.0399</b>
	BodySLAM vs EndoSFMLearner	-4.42	<b>8.71e-05</b>
Squared Relative Error	BodySLAM vs EndoDepth	-2.15	<b>0.0381</b>
	BodySLAM vs EndoSFMLearner	-9.69	<b>1.44e-11</b>
Accuracy (1.25)	BodySLAM vs EndoDepth	5.14	<b>9.69e-06</b>
	BodySLAM vs EndoSFMLearner	2.55	<b>0.0150</b>
Accuracy (1.25) <sup>2</sup>	BodySLAM vs EndoDepth	4.12	<b>0.0002</b>
	BodySLAM vs EndoSFMLearner	1.54	0.1314
Accuracy (1.25) <sup>3</sup>	BodySLAM vs EndoDepth	3.56	<b>0.0011</b>
	BodySLAM vs EndoSFMLearner	1.37	0.1803

**Table 6**

Statistical Performance Analysis of the Monocular Depth Estimation Module on the Hamlyn Dataset. The table details outcomes for Absolute Relative Difference, Root Mean Square Error (RMSE), RMSE Log, Squared Relative Error, and accuracy thresholds (1.25, 1.25<sup>2</sup>, 1.25<sup>3</sup>). Results include pairwise comparisons of BodySLAM versus EndoDepth and BodySLAM versus EndoSFMLearner, assessed through t-tests with a significance level of  $p < 0.05$ .

RMSE, BodySLAM does not statistically outperform EndoSfmLearner; in Squared Relative Error, BodySLAM does not statistically outperform both EndoDepth and EndoSfmLearner; and in Accuracy (1.25)<sup>3</sup>, BodySLAM does not outperform EndoSfmLearner statistically.

## 7. Conclusions

This study presented a robust deep learning-based SLAM approach that can effectively operate across various endoscopic surgical settings, including laparoscopy, gastroscopy, and colonoscopy. We addressed the challenges posed by hardware limitations and environmental variations by integrating deep learning models with strong generalization capabilities into the framework. Our results demonstrate that Zoe’s exceptional generalization abilities, previously showcased in various imaging contexts, can be effectively adapted to the endoscopic field. When compared to current state-of-the-art depth estimation algorithms in endoscopy, Zoe exhibited superior performance, confirming its potential for SLAM applications in surgical environments. These findings are consistent with the results reported by [43]. Another key contribution of our work is the development of a novel unsupervised pose estimation method, CyclePose, based on the CycleGAN architecture. Our comprehensive evaluations revealed CyclePose’s robust generalization capabilities and competitive performance compared to existing state-of-the-art pose estimation techniques, while maintaining the lowest inference time. This makes CyclePose a promising solution for real-time surgical applications. Furthermore, an ablation study conducted on the pose estimation module highlighted

Metric	Comparison	T-Stat	P-Value
Absolute Relative Difference	BodySLAM vs EndoDepth	-9.69	<b>1.44e-11</b>
	BodySLAM vs EndoSFMLearner	-4.14	<b>0.0002</b>
RMSE	BodySLAM vs EndoDepth	-1.01	0.3211
	BodySLAM vs EndoSFMLearner	-0.25	0.8007
RMSE Log	BodySLAM vs EndoDepth	-14.99	<b>4.73e-17</b>
	BodySLAM vs EndoSFMLearner	-8.35	<b>6.04e-10</b>
Squared Relative Error	BodySLAM vs EndoDepth	-0.85	0.4018
	BodySLAM vs EndoSFMLearner	0.31	0.7598
Accuracy (1.25)	BodySLAM vs EndoDepth	13.10	<b>2.92e-15</b>
	BodySLAM vs EndoSFMLearner	5.82	<b>1.22e-06</b>
Accuracy (1.25) <sup>2</sup>	BodySLAM vs EndoDepth	10.13	<b>4.37e-12</b>
	BodySLAM vs EndoSFMLearner	2.56	<b>0.0147</b>
Accuracy (1.25) <sup>3</sup>	BodySLAM vs EndoDepth	8.53	<b>3.65e-10</b>
	BodySLAM vs EndoSFMLearner	1.26	0.2151

**Table 7**

Statistical Performance Analysis of the Monocular Depth Estimation Module on the SCARED Dataset. The table details outcomes for Absolute Relative Difference, Root Mean Square Error (RMSE), RMSE Log, Squared Relative Error, and accuracy thresholds (1.25, 1.25<sup>2</sup>, 1.25<sup>3</sup>). Results include pairwise comparisons of BodySLAM versus EndoDepth and BodySLAM versus EndoSFMLearner, assessed through t-tests with a significance level of  $p < 0.05$ .

the effectiveness of new terms introduced for cycle loss, with the model incorporating the custom term consistently outperforming its counterpart without the term. These considerations are also confirmed by the statistical analysis revealing that Zoe significantly outperformed other depth estimation models in most metrics, with only a few exceptions where the differences were not statistically significant. It also showed that the CyclePose approach performed comparably to other methods while having the lowest inference time, making it a promising solution for real-time surgical applications. Despite these promising results, our study has four limitations. First, although we validated our approach on three relevant endoscopic scenarios, its performance in other settings remains to be investigated. Future research should focus on collecting diverse datasets from a wider range of endoscopic procedures and fine-tuning the deep learning models to adapt to the unique characteristics of each domain, which could help extend the framework’s applicability. Second, the impact of varying illumination conditions and the presence of fluids or debris on the approach’s performance needs further examination. Investigating domain adaptation techniques and developing specialized modules for handling procedure-specific challenges, such as varying illumination and the presence of fluids, could improve the approach’s robustness. Third, the scale ambiguity problem inherent to monocular cameras may affect both the depth estimation and pose estimation modules, resulting in a 3D model that has a scale that differs from the real scale. Exploring methods to mitigate the scale ambiguity problem, such as incorporating

additional sensors or prior knowledge, could enhance the accuracy of depth estimation and pose estimation, and enable more reliable 3D reconstruction validation. Fourth, we have in-silico validated our approach and we are aware that the practical application of the approach in real-world surgical scenarios requires extensive validation and collaboration with medical experts. Conducting rigorous clinical trials involving diverse patient populations and surgical conditions, in close collaboration with medical experts, will be essential for validating the approach's performance and ensuring its seamless integration into the surgical workflow. In spite of these limitations, the proposed SLAM approach has the potential to significantly improve the accuracy and efficiency of endoscopic procedures by providing surgeons with enhanced depth perception and 3D reconstruction capabilities. By addressing the challenges posed by hardware limitations and environmental variations, our deep learning-based framework represents a promising step towards overcoming the limitations of current endoscopic surgical practices. Future research efforts, guided by the identified limitations and potential improvements, can further refine and validate this approach, ultimately leading to its successful integration into clinical practice and improved surgical outcomes for patients.

### CRedit authorship contribution statement

**Guido Manni:** Conceptualization, Methodology, Software, Validation, Formal analysis, Investigation, Writing - Original Draft, Writing - Review and Editing, Visualization. **Clemente Lauretti:** Conceptualization, Methodology, Formal analysis, Writing - Review and Editing, Supervision. **Francesco Prata:** Resources, Data Curation. **Rocco Papalia:** Resources, Data Curation. **Loredana Zollo:** Conceptualization, Methodology, Writing - Review and Editing, Supervision. **Paolo Soda:** Conceptualization, Methodology, Formal analysis, Writing - Review and Editing, Supervision, Project administration, Funding acquisition.

### Declaration of competing interest

The authors declare that they have no known competing financial interests or personal relationships that could have appeared to influence the work reported in this paper.

### Acknowledgements

Guido Manni is a Ph.D. student enrolled in the National Ph.D. in Artificial Intelligence, XXXVII cycle, course on Health and life sciences, organized by Università Campus Bio-Medico di Roma.

This work was partially founded by: i) Piano Nazionale Ripresa e Resilienza (PNRR) - HEAL ITALIA Extended Partnership - SPOKE 2 Cascade Call - "Intelligent Health" with the project BISTOURY - 3D-guided robotic Surgery based on advanced navigation systems and augmented virtual reality (CUP: J33C22002920006); ii) UCBM University Strategic Projects 2023 with the Proof of Concept

(PoC) project BONE - Cooperative Robotic System for spinal surgery; iii) PNRR MUR project PE0000013-FAIR.

### References

- [1] A. Schmidt, O. Mohareri, S. DiMaio, M. C. Yip, S. E. Salcudean, Tracking and mapping in medical computer vision: A review, *Medical Image Analysis* 94 (2024) 103131. doi:<https://doi.org/10.1016/j.media.2024.103131>. URL <https://www.sciencedirect.com/science/article/pii/S1361841524000562>
- [2] A. F. Durrani, G. M. Preminger, Three-dimensional video imaging for endoscopic surgery, *Computers in Biology and Medicine* 25 (2) (1995) 237–247, virtual Reality for Medicine. doi:[https://doi.org/10.1016/0010-4825\(95\)00001-K](https://doi.org/10.1016/0010-4825(95)00001-K). URL <https://www.sciencedirect.com/science/article/pii/001048259500001K>
- [3] L. Stewart, L. W. Way, The prevention of laparoscopic bile duct injuries: An analysis of 300 cases of from a human factors and cognitive psychology perspective, *Proceedings of the Human Factors and Ergonomics Society Annual Meeting* 51 (11) (2007) 617–620. arXiv:<https://doi.org/10.1177/154193120705101103>, doi:10.1177/154193120705101103. URL <https://doi.org/10.1177/154193120705101103>
- [4] R. Smith, K. Schwab, A. Day, T. Rockall, K. Ballard, M. Bailey, I. Jourdan, Effect of passive polarizing three-dimensional displays on surgical performance for experienced laparoscopic surgeons, *British Journal of Surgery* 101 (11) (2014) 1453–1459. arXiv:<https://academic.oup.com/bjs/article-pdf/101/11/1453/36619181/bjs9601.pdf>, doi:10.1002/bjs.9601. URL <https://doi.org/10.1002/bjs.9601>
- [5] N. Vettoretto, E. Foglia, L. Ferrario, A. Arezzo, R. Cirocchi, G. Corullo, G. Currò, D. Marchi, G. Portale, C. Gerardi, U. Nocco, M. Tringali, G. Anania, M. Piccoli, G. Silecchia, M. Morino, A. Valeri, E. Lettieri, Why laparoscopists may opt for three-dimensional view: a summary of the full hta report on 3d versus 2d laparoscopy by s.i.c.e. (società italiana di chirurgia endoscopica e nuove tecnologie), *Surgical Endoscopy* 32 (6) (2018) 2986–2993. doi:10.1007/s00464-017-6006-y. URL <https://doi.org/10.1007/s00464-017-6006-y>
- [6] S. M. D. Sørensen, M. M. Savran, L. Konge, F. Bjerrum, Three-dimensional versus two-dimensional vision in laparoscopy: a systematic review, *Surgical Endoscopy* 30 (1) (2016) 11–23. doi:10.1007/s00464-015-4189-7. URL <https://doi.org/10.1007/s00464-015-4189-7>
- [7] S. Davies, M. Ghallab, S. Hajibandeh, S. Hajibandeh, S. Addison, Three-dimensional versus two-dimensional imaging during laparoscopic cholecystectomy: a systematic review and meta-analysis of randomised controlled trials, *Langenbeck's Archives of Surgery* 405 (5) (2020) 563–572. doi:10.1007/s00423-020-01909-9. URL <https://doi.org/10.1007/s00423-020-01909-9>
- [8] K. Schwab, R. Smith, V. Brown, M. Whyte, I. Jourdan, Evolution of stereoscopic imaging in surgery and recent advances, *World Journal of Gastrointestinal Endoscopy* 9 (8) (2017) 368–377. doi:10.4253/wjge.v9.i8.368. URL <https://doi.org/10.4253/wjge.v9.i8.368>
- [9] T. Bergen, T. Wittenberg, Stitching and surface reconstruction from endoscopic image sequences: A review of applications and methods, *IEEE Journal of Biomedical and Health Informatics* 20 (1) (2016) 304–321. doi:10.1109/JBHI.2014.2384134. URL <https://doi.org/10.1109/JBHI.2014.2384134>
- [10] S. Bano, F. Vasconcelos, A. L. David, J. Deprest, D. Stoyanov, Placental vessel-guided hybrid framework for fetoscopic mosaicking, *Computer Methods in Biomechanics and Biomedical Engineering: Imaging & Visualization* 11 (4) (2023) 1166–1171. arXiv:<https://doi.org/10.1080/21681163.2022.2154278>, doi:10.1080/21681163.2022.2154278. URL <https://doi.org/10.1080/21681163.2022.2154278>

- [11] L. Li, S. Bano, J. Deprest, A. L. David, D. Stoyanov, F. Vasconcelos, Globally optimal fetoscopic mosaicking based on pose graph optimisation with affine constraints, *IEEE Robotics and Automation Letters* 6 (4) (2021) 7831–7838. doi:10.1109/LRA.2021.3100938. URL <https://doi.org/10.1109/LRA.2021.3100938>
- [12] R. Arandjelovic, P. Gronat, A. Torii, T. Pajdla, J. Sivic, Netvlad: Cnn architecture for weakly supervised place recognition, in: 2016 IEEE Conference on Computer Vision and Pattern Recognition (CVPR), 2016, pp. 5297–5307. doi:10.1109/CVPR.2016.572. URL <https://doi.org/10.1109/CVPR.2016.572>
- [13] A. R. Widya, Y. Monno, M. Okutomi, S. Suzuki, T. Gotoda, K. Miki, Stomach 3d reconstruction based on virtual chromoendoscopic image generation, in: 2020 42nd Annual International Conference of the IEEE Engineering in Medicine & Biology Society (EMBC), 2020, pp. 1848–1852. doi:10.1109/EMBC44109.2020.9176016. URL <https://doi.org/10.1109/EMBC44109.2020.9176016>
- [14] M. N. Cheema, A. Nazir, B. Sheng, P. Li, J. Qin, J. Kim, D. D. Feng, Image-aligned dynamic liver reconstruction using intra-operative field of views for minimal invasive surgery, *IEEE Transactions on Biomedical Engineering* 66 (8) (2019) 2163–2173. doi:10.1109/TBME.2018.2884319. URL <https://doi.org/10.1109/TBME.2018.2884319>
- [15] S. Zhang, L. Zhao, S. Huang, R. Ma, B. Hu, Q. Hao, 3d reconstruction of deformable colon structures based on preoperative model and deep neural network, in: 2021 IEEE International Conference on Robotics and Automation (ICRA), 2021, pp. 1875–1881. doi:10.1109/ICRA48506.2021.9561772. URL <https://doi.org/10.1109/ICRA48506.2021.9561772>
- [16] K. B. Ozyoruk, G. I. Gokceler, T. L. Bobrow, G. Coskun, K. Inctan, Y. Almalioglu, F. Mahmood, E. Curto, L. Perdigoto, M. Oliveira, H. Sahin, H. Araujo, H. Alexandrino, N. J. Durr, H. B. Gilbert, M. Turan, Endoslam dataset and an unsupervised monocular visual odometry and depth estimation approach for endoscopic videos, *Medical Image Analysis* 71 (2021) 102058. doi:https://doi.org/10.1016/j.media.2021.102058. URL <https://www.sciencedirect.com/science/article/pii/S1361841521001043>
- [17] D. Recasens, J. Lamarca, J. M. Fácil, J. M. M. Montiel, J. Civera, Endo-depth-and-motion: Reconstruction and tracking in endoscopic videos using depth networks and photometric constraints, *IEEE Robotics and Automation Letters* 6 (4) (2021) 7225–7232. doi:10.1109/LRA.2021.3095528. URL <https://doi.org/10.1109/LRA.2021.3095528>
- [18] X. Liu, Z. Li, M. Ishii, G. D. Hager, R. H. Taylor, M. Unberath, Sage: Slam with appearance and geometry prior for endoscopy, in: 2022 International Conference on Robotics and Automation (ICRA), 2022, pp. 5587–5593. doi:10.1109/ICRA46639.2022.9812257. URL <https://doi.org/10.1109/ICRA46639.2022.9812257>
- [19] A. R. Widya, Y. Monno, M. Okutomi, S. Suzuki, T. Gotoda, K. Miki, Whole stomach 3d reconstruction and frame localization from monocular endoscope video, *IEEE Journal of Translational Engineering in Health and Medicine* 7 (2019) 1–10. doi:10.1109/JTEHM.2019.2946802. URL <https://doi.org/10.1109/JTEHM.2019.2946802>
- [20] K. Makki, K. Chandelon, A. Bartoli, Elliptical specularly detection in endoscopy with application to normal reconstruction, *International Journal of Computer Assisted Radiology and Surgery* 18 (7) (2023) 1323–1328. doi:10.1007/s11548-023-02904-3. URL <https://doi.org/10.1007/s11548-023-02904-3>
- [21] S. Zhang, L. Zhao, S. Huang, H. Wang, Q. Luo, Q. Hao, Slam-tka: Real-time intra-operative measurement of tibial resection plane in conventional total knee arthroplasty, in: L. Wang, Q. Dou, P. T. Fletcher, S. Speidel, S. Li (Eds.), *Medical Image Computing and Computer Assisted Intervention – MICCAI 2022*, Springer Nature Switzerland, Cham, 2022, pp. 126–135. doi:10.1007/978-3-031-16449-1\_13. URL [https://doi.org/10.1007/978-3-031-16449-1\\_13](https://doi.org/10.1007/978-3-031-16449-1_13)
- [22] J. Schüle, J. Haag, P. Somers, C. Veil, C. Tarín, O. Sawodny, A model-based simultaneous localization and mapping approach for deformable bodies, in: 2022 IEEE/ASME International Conference on Advanced Intelligent Mechatronics (AIM), 2022, pp. 607–612. doi:10.1109/AIM52237.2022.9863308. URL <https://doi.org/10.1109/AIM52237.2022.9863308>
- [23] Y. Li, F. Richter, J. Lu, E. K. Funk, R. K. Orosco, J. Zhu, M. C. Yip, Super: A surgical perception framework for endoscopic tissue manipulation with surgical robotics, *IEEE Robotics and Automation Letters* 5 (2) (2020) 2294–2301. doi:10.1109/LRA.2020.2970659. URL <https://doi.org/10.1109/LRA.2020.2970659>
- [24] Z. Liu, W. Gao, J. Zhu, Z. Yu, Y. Fu, Surface deformation tracking in monocular laparoscopic video, *Medical Image Analysis* 86 (2023) 102775. doi:https://doi.org/10.1016/j.media.2023.102775. URL <https://www.sciencedirect.com/science/article/pii/S1361841523000361>
- [25] Stereo correspondence and reconstruction of endoscopic data sub-challenge, <https://endovissub2019-scared.grand-challenge.org/>, accessed: 2024-06-17 (2019).
- [26] E. Rublee, V. Rabaud, K. Konolige, G. Bradski, Orb: An efficient alternative to sift or surf, in: 2011 International Conference on Computer Vision, 2011, pp. 2564–2571. doi:10.1109/ICCV.2011.6126544. URL <https://doi.org/10.1109/ICCV.2011.6126544>
- [27] D. G. Lowe, Distinctive image features from scale-invariant keypoints, *International Journal of Computer Vision* 60 (2) (2004) 91–110. doi:10.1023/B:VISI.0000029664.99615.94. URL <https://doi.org/10.1023/B:VISI.0000029664.99615.94>
- [28] H. Bay, T. Tuytelaars, L. Van Gool, Surf: Speeded up robust features, in: A. Leonardis, H. Bischof, A. Pinz (Eds.), *Computer Vision – ECCV 2006*, Springer Berlin Heidelberg, Berlin, Heidelberg, 2006, pp. 404–417. doi:10.1007/11744023\_32. URL [https://doi.org/10.1007/11744023\\_32](https://doi.org/10.1007/11744023_32)
- [29] B. Triggs, P. F. McLauchlan, R. I. Hartley, A. W. Fitzgibbon, Bundle adjustment — a modern synthesis, in: B. Triggs, A. Zisserman, R. Szeliski (Eds.), *Vision Algorithms: Theory and Practice*, Springer Berlin Heidelberg, Berlin, Heidelberg, 2000, pp. 298–372. doi:10.1007/3-540-44480-7\_21. URL [https://doi.org/10.1007/3-540-44480-7\\_21](https://doi.org/10.1007/3-540-44480-7_21)
- [30] N. Mahmoud, A. Hostettler, T. Collins, L. Soler, C. Doignon, J. Montiel, Slam based quasi dense reconstruction for minimally invasive surgery scenes (05 2017).
- [31] Q. Zhao, T. Price, S. Pizer, M. Niethammer, R. Alterovitz, J. Rosenman, The endoscopogram: A 3d model reconstructed from endoscopic video frames, in: S. Ourselin, L. Joskowicz, M. R. Sabuncu, G. Unal, W. Wells (Eds.), *Medical Image Computing and Computer-Assisted Intervention – MICCAI 2016*, Springer International Publishing, Cham, 2016, pp. 439–447. doi:10.1007/978-3-319-46720-7\_51. URL [https://doi.org/10.1007/978-3-319-46720-7\\_51](https://doi.org/10.1007/978-3-319-46720-7_51)
- [32] R. Chen, T. Bobrow, T. Athey, F. Mahmood, N. Durr, Slam endoscopy enhanced by adversarial depth prediction (06 2019).
- [33] C. Godard, O. M. Aodha, M. Firman, G. Brostow, Digging into self-supervised monocular depth estimation, in: 2019 IEEE/CVF International Conference on Computer Vision (ICCV), 2019, pp. 3827–3837. doi:10.1109/ICCV.2019.00393. URL <https://doi.org/10.1109/ICCV.2019.00393>
- [34] G. Klein, D. Murray, Parallel tracking and mapping for small ar workspaces, in: 2007 6th IEEE and ACM International Symposium on Mixed and Augmented Reality, 2007, pp. 225–234. doi:10.1109/ISMAR.2007.4538852. URL <https://doi.org/10.1109/ISMAR.2007.4538852>
- [35] S. Bhat, R. Birkel, D. Wofk, P. Wonka, M. Mueller, Zoedepth: Zero-shot transfer by combining relative and metric depth (02 2023).
- [36] D. Ho, K. Rao, Z. Xu, E. Jang, M. Khansari, Y. Bai, Retinagan: An object-aware approach to sim-to-real transfer, in: 2021 IEEE International Conference on Robotics and Automation (ICRA), 2021, pp. 10920–10926. doi:10.1109/ICRA48506.2021.9561157. URL <https://doi.org/10.1109/ICRA48506.2021.9561157>

- [37] X. Chen, Y. Duan, R. Houthoofd, J. Schulman, I. Sutskever, P. Abbeel, Infogan: Interpretable representation learning by information maximizing generative adversarial nets, in: D. Lee, M. Sugiyama, U. Luxburg, I. Guyon, R. Garnett (Eds.), *Advances in Neural Information Processing Systems*, Vol. 29, Curran Associates, Inc., 2016. URL [https://proceedings.neurips.cc/paper\\_files/paper/2016/file/7c9d0b1f96aebd7b5eca8c3edaa19ebb-Paper.pdf](https://proceedings.neurips.cc/paper_files/paper/2016/file/7c9d0b1f96aebd7b5eca8c3edaa19ebb-Paper.pdf)
- [38] R. Ranftl, K. Lasinger, D. Hafner, V. Koltun, Towards robust monocular depth estimation: Mixing datasets for zero-shot cross-dataset transfer, *IEEE Transactions on Pattern Analysis and Machine Intelligence* PP (2020) 1–1. doi:10.1109/TPAMI.2020.3019967.
- [39] B. Curless, M. Levoy, A volumetric method for building complex models from range images, *Proceedings of the 23rd annual conference on Computer graphics and interactive techniques* (1996).
- [40] N. Mayer, E. Ilg, P. Häusser, P. Fischer, D. Cremers, A. Dosovitskiy, T. Brox, A large dataset to train convolutional networks for disparity, optical flow, and scene flow estimation, in: *2016 IEEE Conference on Computer Vision and Pattern Recognition (CVPR)*, 2016, pp. 4040–4048. doi:10.1109/CVPR.2016.438. URL <https://doi.org/10.1109/CVPR.2016.438>
- [41] A. Masoumian, H. A. Rashwan, J. Cristiano, M. S. Asif, D. Puig, Monocular depth estimation using deep learning: A review, *Sensors* 22 (14) (2022). doi:10.3390/s22145353. URL <https://www.mdpi.com/1424-8220/22/14/5353>
- [42] Q.-Y. Zhou, V. Koltun, Dense scene reconstruction with points of interest, *ACM Transactions on Graphics* 32 (07 2013). doi:10.1145/2461912.2461919.
- [43] J. J. Han, A. Acar, C. Henry, J. Y. Wu, Depth anything in medical images: A comparative study (2024). arXiv:2401.16600. URL <https://arxiv.org/abs/2401.16600>